The effect of fiber concentration on fiber orientation in injection molded film gated rectangular plates

Jens Kjær Jørgensen[a], Erik Andreassen[a] and Dietmar Salaberger[b]

[a]SINTEF Materials and Chemistry, Forskningsveien 1, 0314 Oslo, Norway

[b] Dietmar Salaberger, University Of Applied Sciences Upper Austria, Stelzhamerstraße. 23, 4600 Wels, Austria.

Parts of the result presented here was presented orally at the Polymer Processing Society European conference in Graz, 2015.

The effect of fiber concentration on fiber orientation in injection molded film gated rectangular plates

Jens Kjær Jørgensen[a], Erik Andreassen[a] and Dietmar Salaberger[b]

[a]SINTEF Materials and Chemistry, Forskningsveien 1, 0314 Oslo, Norway

[b] Dietmar Salaberger, University Of Applied Sciences Upper Austria, Stelzhamerstraße. 23, 4600 Wels, Austria.

Abstract

Fiber orientation in film gated injection-molded rectangular plates was characterized using micro computed tomography. Polyamide 12 materials with 15, 30 and 50 wt% glass fibers were used in this study. For all three materials, the typical core-shell layer structure of fiber orientation was observed, but several features of the fiber orientation were highly dependent on the fiber content. Increasing fiber content resulted in increasing core layer thickness and a higher degree of orientation in the shell layer. These effects may be associated with plug flow induced by extra stress from the fibers, which changes the melt rheology compared to non-filled material. The Dinh-Armstrong model for the fiber-induced extra stress could not explain the fiber content dependencies. This appears to be attributed to the uncertainty in determining the particle number N_p for the high fiber concentrations present in the samples. Analyses of fiber orientation as a function of fiber length revealed a dependence on fiber length in qualitative agreement with Jeffery's model for fiber dynamics.

Abbreviations:

SFRT: Short fiber reinforced thermoplastics

μ-CT: micro computed (X-ray) tomography

HD: Hydrodynamic

FT: Folgar–Tucker

IRD: Isotropic rotary diffusion

ARD: Anisotropic rotary diffusion

RSC :Reduced strain closure

PA15, PA30, PA50 : Polyamide 12 with 15, 30 and 50 wt% fiber

Introduction

Injection molded short fiber reinforced thermoplastics (SFRT) is a class of engineering materials used in applications requiring moderate to high strength and stiffness, low weight and reasonable production costs. The mechanical properties of injection molded SFRT components are governed by the orientation of the fibers in the polymer matrix, which in turn is a result of the interaction between the fibers and the flow of the polymer melt during the molding process. A substantial amount of research has been devoted to understanding the interaction between polymer flow and the development of fiber orientation [1]. This has led to the development of numerical models for flow-induced fiber orientation which today are standard in commercial injection molding software. It is well known that in general there can be a strong coupling between fiber orientation and flow for fiber-filled thermoplastics. During flow, the fibers will resist any stretching along its axis. This resistance makes the rheological properties of the SFRT melt anisotropic. Therefore, not only is the fiber orientation dependent on the flow history, but the flow also depends on the instant fiber orientation. Nevertheless, because it is computationally intensive, this coupling is often ignored in numerical simulations, and, as will be discussed further on, this is a reasonable assumption in some cases, but not in all.

The objective of this work is to study the influence of fiber concentration on fiber orientation and the role of fiber–flow coupling in that context. Film gated rectangular plates with the same polymer with varying fiber content was injection molded. Subsequently the fiber orientation in selected regions of the plates were determined using micro computed x-ray tomography (μ-CT). Experimental observations are the primary objective of this paper. In addition, the results are discussed in relation to the most accepted models for fiber orientation development in SFRT, involving flow-induced fiber dynamics and fiber-flow coupling. Before reviewing the existing knowledge on this subject, the basic relationships between fiber orientation distributions and orientation tensors are summarized.

Orientation tensors

The orientation of a fiber can be described by a unit vector $\mathbf{p}$ along its axis. However, when regarding the SFRT as a continuum material one does not consider the orientation of single fibers, but rather a 3D fiber orientation distribution $\psi(\mathbf{p})$ at given points or sub volumes. Nevertheless, using $\psi(\mathbf{p})$ in numerical calculations is computationally intensive. Hence, Advani and Tucker [2] introduced the use of orientation tensors to provide an approximate

representation of $\psi(\mathbf{p})$. The second order and fourth order orientation tensors **A** and $\mathbf{A_4}$ are defined as

$$\mathbf{A} = \int \psi(\mathbf{p})\mathbf{pp}d\mathbf{p} \quad , \quad \mathbf{A}_4 = \int \psi(\mathbf{p})\mathbf{pppp}d\mathbf{p} \tag{1}$$

The second order orientation tensor has proved to be an efficient tool for comparing simulated and experimentally determined fiber orientations

The components of **A,** A_{ij}, can be represented in the form of a symmetric matrix

$$\mathbf{A} = \sum_{i,j=1}^{3} A_{ij}\mathbf{e_i}\mathbf{e_j} \quad , A_{ij} = \begin{bmatrix} a_{11} & a_{12} & a_{13} \\ a_{12} & a_{22} & a_{23} \\ a_{13} & a_{23} & a_{33} \end{bmatrix} \tag{2}$$

with trace $a_{11} + a_{22} + a_{33} = 1$. Here $\mathbf{e_i}\mathbf{e_j}$ is the dyadic product of the coordinate system unit vectors.

A useful property of **A,** as for any symmetric matrixes, is that it has three orthogonal eigenvectors $\bar{\mathbf{e}}_\mathbf{i}$ with corresponding eigenvalues λ_i. In a Cartesian coordinate system with axes parallel to the eigenvectors only the diagonal components are non-zero, and these are the eigenvalues such that

$$\mathbf{A} = \sum_{i,j=1}^{3} \bar{A}_{ij}\bar{\mathbf{e}}_\mathbf{i}\bar{\mathbf{e}}_\mathbf{i} = \sum_{i=1}^{3} \lambda_i \bar{\mathbf{e}}_\mathbf{i}\bar{\mathbf{e}}_\mathbf{i} \quad , \quad \bar{A}_{ij} = \begin{bmatrix} \lambda_1 & 0 & 0 \\ 0 & \lambda_2 & 0 \\ 0 & 0 & \lambda_3 \end{bmatrix} \tag{3}$$

Here the bar refers to the coordinate system parallel with the eigenvectors.

For the orientation tensor, the eigenvectors and eigenvalues are also referred to as principal axis of orientation and principal orientations components respectively.

A useful way to visualize the orientation tensor is a "tensor cross" of three lines in the direction of the principal axis of orientation with length proportional to the principal orientations components, or alternatively as ellipsoids with the same three lines as 1st, 2nd and 3rd axis. In this paper "tensor crosses" will be used. These "tensor crosses" serve as a graphical simplification of the orientation distribution as illustrated in Figure 1, where a typical fiber orientation distribution is overlaid with the corresponding "tensor cross". For

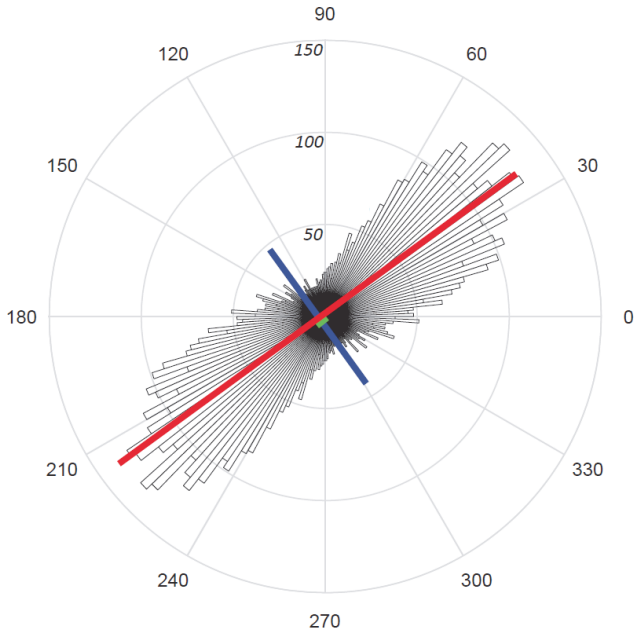

Figure 1 A fiber orientation distribution (in black) and the corresponding "tensor cross" (in red, blue and green) with axes parallel to the principal directions and axis length proportional to the corresponding principal orientations component. Both cases are three dimensional, but here viewed along the third principal direction for easier comparison.

simplicity, the figure shows the projection onto a 2D plane. Note that the orientation distribution is inherently symmetric around ±180 °.

Flow-fiber interaction

Several reviews of the interaction between flow and fiber orientation development can found in the literature, e.g. the paper by Laure et al. [1]. Fibers are aligned by both shear flow and extensional flow. In shear flow, fibers preferentially align in the shear plane along the shearing direction. In extensional (stretching) flow, the fibers orient along the direction of stretching. Injection molding is dominated by shear flow, but extensional flows also occur. Contractions and expansions in the cavity induce strong extensional flows that orient fibers along and transverse to the flow direction, respectively. The flow front is characterized by a fountain flow with flow vectors angled towards the walls, resulting in an extensional flow component in the through-thickness (z) direction [3]. For many injection molded parts the major part of the filling can be approximated as flow between two parallel plates. Upstream from the flow front, such a flow is characterized by a high shear rate in a zone close to the wall. The shear rate gradually decreases to zero towards the center of the cavity. If the flow is divergent, the flow will also have a transverse extensional component. The classical example

of a divergent flow is the filling of a center-gated disc, where the flow front area expands radially from the gate. Divergent flow is present in the filling of all point-gated cavities and in most other cases where the flow is not confined to one direction. Shear in the filling direction will dominate in the zone close to the wall, while transverse extension will be dominant in the core. In between, there will be a mix of shear and extensional flow. Downstream from the gate in a long film gated rectangular strip, flow lines will become almost parallel and transverse extensional flow will cease.

The fiber orientation resulting from the flow between two parallel mold cavity walls is a core-shell structure with a shell layer of fibers aligned in the filling direction and a core layer with transversely aligned fibers. Between the core and shell layers a transition layer with more random orientation exist. The skin of a molded part contains fibers which were deposited directly from the fountain flow at the flow front and they are randomly oriented in the plane parallel to the cavity plane. Figure 2 provides a schematic illustration of this layered structure. In the flow front region the orientation is rather random with significant orientation in the through-thickness direction [3].

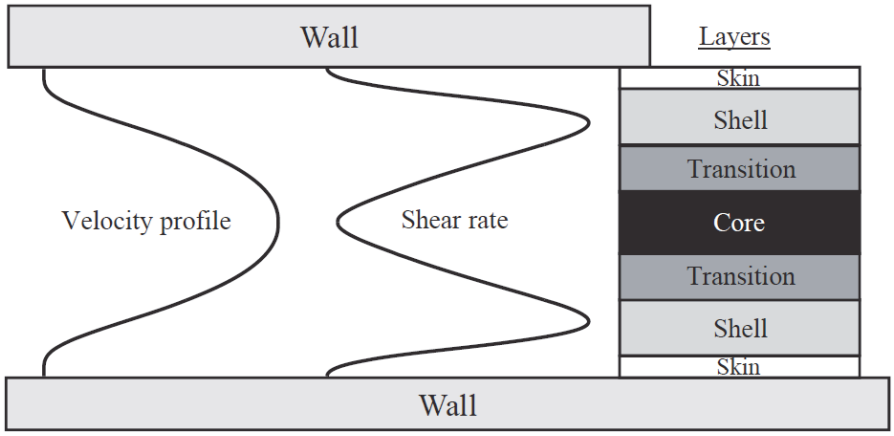

Layer name	*Orientation*	*Source of orientation*
Skin	Random in cavity plane	Deposition from flow front onto cold wall
Shell	Aligned with filling direction	Shear flow
Transition	No preferential	Mixed shear and extensional
Core	Transverse to filling direction	Extensional flow

Figure 2 Schematic illustration of the through-thickness velocity and shear rate profiles between two parallel cavity walls in injection molding, and the resulting layered fiber orientation structure.

The relative thickness of the shell layer increases as the cavity thickness decreases. Hence, the relative thickness of the core layer decreases with decreasing wall thickness [4, 5]. If the flow is non-divergent and transverse extensional flow is weak or absent, as for instance in a film gated strip, the core orientation will be more random and dependent on the upstream flow field [5].

Fiber dynamic models

The starting point for the fiber dynamic models considered here is Jeffery's hydrodynamic equation for the motion of a single ellipsoidal particle, representing a fiber, in a flow field [6, 7]

$$\dot{\mathbf{p}} = \mathbf{W}\cdot\mathbf{p} + \lambda\left(\mathbf{D}\cdot\mathbf{p} - \mathbf{D}:\mathbf{ppp}\right)$$
$$\lambda = \frac{a_r^{\,2}-1}{a_r^{\,2}+1} \qquad (4)$$

Here $\mathbf{p}$ is the unit orientation vector of the fiber, $\dot{\mathbf{p}}$ the material derivative of $\mathbf{p}$ and $\mathbf{W}$ and $\mathbf{D}$ the vorticity tensor and rate of deformation tensor, respectively. ($D_{ij} = ½(v_{i,j} + v_{j,i})$ and $W_{ij} = ½(v_{i,j} - v_{j,i})$. The factor λ is a shape factor dependent on the aspect ratio a_r. This factor is close to 1 for most practical cases. Consider a single fiber in a simple shear flow with shear rate $\dot{\gamma}$, oriented with angle $\phi(t)$, where ϕ *is* defined as zero when the fiber is aligned in the direction of the shear gradient. According to Jeffery's model this fiber will be subjected to a rolling motion with variable angular speed given as (equation 47 in Jeffery's original paper [6])

$$\frac{d\phi}{dt} = \frac{\dot{\gamma}}{a_r^{\,2}+1}\left(a_r^{\,2}\cos^2\phi + \sin^2\phi\right) \qquad (5)$$

The angular velocity is lowest when the fiber lies in the shear plane and highest when the fiber is aligned with the shear gradient. The ratio of the angular velocities for these two cases is proportional to a_r^2. Hence, on average, the fiber is predicted to be mostly oriented along the shear direction and this preferred orientation becomes increasingly more dominant with increasing a_r.

The most widely accepted and used model for the evaluation of the second order orientation tensor is the Folgar–Tucker (FT) model that was develop by combining Jeffery's model, rotary diffusion and the concept of orientation tensors [2, 8]. The FT model is stated as

$$
\begin{aligned}
\dot{\mathbf{A}}^{FT} &= \dot{\mathbf{A}}^{HD} + \dot{\mathbf{A}}^{IRD} \\
\dot{\mathbf{A}}^{HD} &= \left(\mathbf{W}\cdot\mathbf{A} - \mathbf{A}\cdot\mathbf{W}\right) + \lambda\left(\mathbf{D}\cdot\mathbf{A} + \mathbf{A}\cdot\mathbf{D} - 2\mathbf{A}_4 : \mathbf{D}\right) \\
\dot{\mathbf{A}}^{IRD} &= 2\dot{\gamma}C_I\left(\mathbf{I} - 3\mathbf{A}\right) \\
\dot{\gamma} &= \sqrt{2\mathbf{D} : \mathbf{D}}
\end{aligned}
\tag{6}
$$

Here $\dot{\mathbf{A}}^{FT}$ is the FT rate of change of **A,** which is the sum of a hydrodynamic induced rate of change (HD) corresponding to Jeffery's model, and a rate of change due to isotropic rotary diffusion (IRD). The IRD term was introduced based on experimental observations showing that the HD model predicted a too high degree of orientation in sheared regions [8]. The function of the IRD term is to drive all anisotropic orientations toward isotropy. The IRD rate is proportional to the rate of deformation and the coefficient C_I. The physical interpretation of the rotary diffusion is that it originates from interaction between fibers. Jeffery's model is based on isolated fibers, while in real fiber suspensions fibers are influenced by fiber-fiber interaction and random hydrodynamic forces generated by movement of adjacent fibers. Hence, C_I is referred to as the interaction coefficient. Appropriate values of C_I are in the range 0.0001- 0.05. Comparisons of injection molding simulations and experiments suggest that C_I decreases with increasing fiber concentration [5]. Contrary to this, direct numerical simulations of fiber-fiber interactions have suggested the opposite [9].

The introduction of the IRD term has been a success, but the predictions with the FT model still deviate from experimental observations. A slower rate of orientation development and a thicker core layer with a more gradual transition is observed in experiments when compared to the FT model predictions [4, 5, 10]. Slower kinetics for the orientation has been accounted for by multiplying $\dot{\mathbf{A}}^{FT}$ by a strain reduction factor [11] or slip coefficient [12], which downscale the strain experienced by the fibers. However, as stressed by Wang et al. [13] this approach is not objective with respect to the coordinate system. Hence, Wang et al. developed the more theoretically thorough Reduced Strain Closure (RSC) model incorporating a coordinate-objective reduced orientation rate [13]. Kleindel et al. [14] evaluated the performance of the FT-RSC model compared to only FT model in simulations of a complex part with chunky geometry. The simulation where evaluated towards fiber orientation detemined by μ-CT. RSC improved the prediction of core thickness but the degree of orientation transverse to flow in the core was underestimated.

The IRD term can be tuned to reduce the high degree of orientation predicted from the HD term, along the flow direction in the highly shear strained shell layer, by "pushing" fibers to

all other directions. However, the IRD term has been found to give too high out-of-plane orientation and too low orientation in the in-plane transverse to flow direction [5, 10, 15-17]. To overcome this limitation of the FT model, Phelps and Tucker introduced the anisotropic rotary diffusion model (ARD) [10]. Anisotropic rotary diffusion implies that some directions are more prone to rotary diffusion than others. For instance, there is more diffusion from the "flow direction" to the "in plane transverse to flow direction" than to the "out of plane/through-thickness direction". Models comparable to the ARD and RSC models have been formulated by Tseng et al. [18, 19].

Fiber-flow coupling

Papers reporting experimental findings on the effect of fiber concentration on fiber orientation in injection molding are scarce. Kim et al. [20] compared the fiber orientation in slender plates molded with 30, 50 and 70 wt% long fiber polypropylene. However, their discussion is limited and lacks conclusions. Lipscomp et al. [21] presented experimental images showing strong fiber-flow coupling for fibers suspended in a Newtonian oil during flow through a contraction. The fibers gave rise to much straighter streamlines, and significantly increased the size of the corner vortex. Lipscomp et al. did not measure the fiber orientation, but the strong effect on the flow would obviously influence the resulting orientation. In contrast, the effect of fibers on rheology has been the subjected to a significant amount of theoretical and numerical studies. The stress $\boldsymbol{\sigma}$ in an incompressible fiber suspension flow can be formulated as

$$\boldsymbol{\sigma} = p\mathbf{I} + 2\eta\mathbf{D} + \mathbf{T}^{fiber} \tag{7}$$

Here p is the pressure, η the fluid viscosity, $\mathbf{D}$ the rate of deformation tensor and $\mathbf{T}^{fiber}$ is the extra stress contribution from the fibers. According to Dinh and Armstrong [22] the extra stress is mainly due to viscous drag between the polymer and the fibers, parallel to the fiber axes, and can be modelled as

$$\mathbf{T}^{fiber} = 2\eta N_p \mathbf{D} : \mathbf{A}_4 \Leftrightarrow T_{ij}^{fiber} = 2\eta N_p D_{kl} A_{ijkl} \tag{8}$$

Here N_p is a dimensionless coefficient called the particle number, given as

$$N_p = \frac{c\left(L_f / D_f\right)^2}{3\ln\left(2h_f / D_f\right)} \tag{9}$$

where c, L_f, D_f and h_f are the fiber volume fraction, fiber length, fiber diameter and average lateral fiber–fiber spacing, respectively. Since h_f depends on the fiber orientation, N_p is also orientation dependent. Equation 8 was developed for the semi-concentrated regime $a_r^{-2} < c < a_r^{-1}$ (a_r is fiber aspect ratio L_f/D_f). Nevertheless, it is frequently applied for higher concentrations. Note that for a simple shear flow Equation 8 predicts no extra stress for fibers oriented in the shear plane and a maximum in extra stress for fibers oriented 45° to the shear gradient direction. In extensional flow, mainly the fibers oriented in the stretching direction contribute to the extra stress $\mathbf{T}^{fiber}$.

Laun [23] and Eberle et al. [24] performed measurements that qualitatively validate Equation 8. In the start-up of shear flow, an overshoot peak in the shear stress and the normal stress difference occurs at low strains followed by a gradual decay to steady state. This stress peak is associated to a reorganization of the fibers. During this reorganization, the fibers rotate through the 45° orientation, where they provide maximum extra stress, followed by gradually higher alignment in the shear plane, and a decay of the extra stress. The overshoots increase with fiber concentration [23, 24] and fiber aspect ratio [23]. Laun [23] also compared the viscosity of unfilled and fiber-filled polymers for a large range of shear rates. At high rates, a similar degree of shear thinning was observed with and without fibers. At low rates, the unfilled polymers reached a plateau (zero shear viscosity) while the fiber-filled materials exhibited a steep increase of viscosity with decreasing shear rate comparable to a material with yield stress. Thus, the fiber-filled material showed a higher degree of shear thinning. In general, the tendency for plug flow in injection molding increases with increasing level of shear thinning. Hence, fiber-filled materials are expected to be more prone to plug flow compared to the same material without fibers. Tucker [25] showed, through a qualitative study of the governing equations, that for narrow gap shear flow, even a small out of plane fiber orientation component can increase flow resistance and generate either plug flow or bell shaped flow profiles, depending on the through-thickness position of the fibers aligned out of plane.

VerWeyst and Tucker [26] performed flow simulations with fiber-flow coupling, using the same contraction geometry and fluid as studied experimentally by Lipscomp and discussed above [21]. Good agreement was found with Lipscomps observation of vortices and flow

lines for both the unfilled and fiber-filled case using $N_p = 6$ for the filled case, as proposed by Lipscomp. Similar results were obtained by Redjeb et al. [27] in decoupled and coupled (N_p = 10) simulations of a contraction.

Coupled flow in discs or plates with parallel walls have been studied analytically by Tucker [25], and by numerical simulations by several authors [4, 15, 26-29]. These studies predict that fibers can promote both plug flows [4, 25, 27] and bell-shaped velocity profiles with increased center layer velocity [15, 25, 26, 28]. Mazahir pointed out [15] that differences in the fiber orientation at the inlet is a probable cause for these different results and thus inlet fiber orientation should be chosen carefully. Also, it is important to include the fountain flow to capture the coupling effect at the flow front [29].

Materials and samples

Three glass fiber reinforced PA12 materials commercially available as Grilamid LV15, LV30 and LV50 (EMS-Grivory Switzerland) were used in this study. The materials contain the same PA12 matrix material and nominally 15, 30 and 50 wt% fibers, respectively. The actual fiber wt% and V% were estimated from pyrolysis (550˚C for 1h) of samples with known density and using 2.54 g/cm^2 as density for glass fiber. These values are listed in *Table 1*. The materials will be termed PA15, PA30 and PA50 and referred to with their nominal weight fractions throughout this paper.

The geometry of the specimens studied in this work is a rectangular film gated plate with dimensions 80 mm × 80 mm × 4 mm, as shown in Figure 3. Plates were molded using a Battenfeld EM 50/120 injection molding machine (Wittmann Battenfeld GmbH, Austria) with the following processing settings: Filling rate 65 cm^3/s, melt temperature 270 °C, mold temperature 80 °C and holding pressure 400 bar. Samples for μ-CT scans where cut out from positions along the midline of the plates at distance 0, 6, 10, 28 and 50 mm from the inlet, as shown in Figure 3.

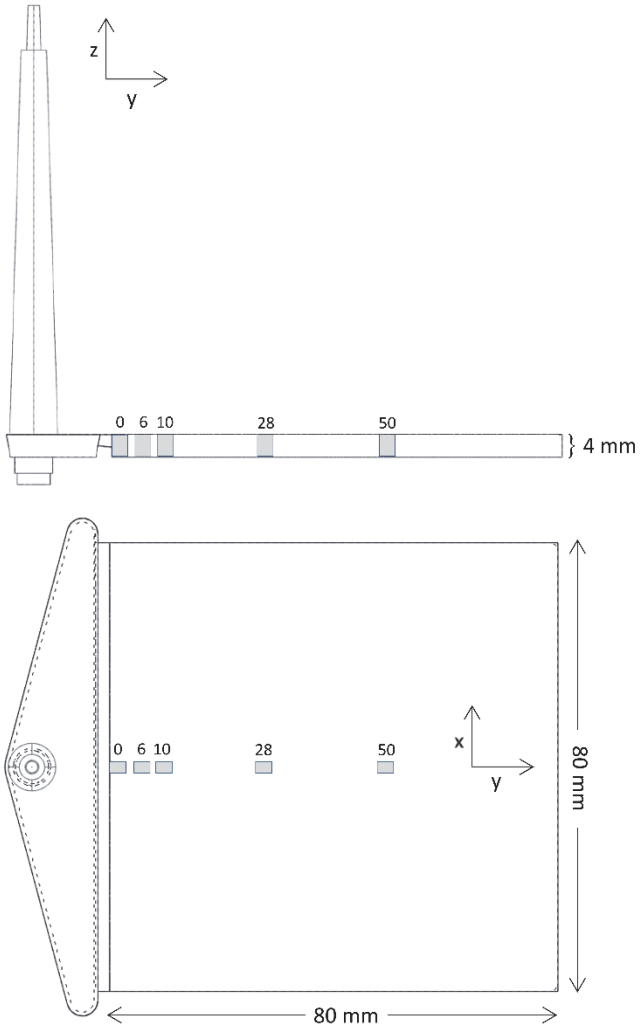

Figure 3 Geometry of the injection molded specimens with specification of coordinate directions. The positions of the samples analyzed with μ-CT are marked in the figure.

Fiber orientation and length measurements

X-ray CT scans were performed with a Nanotom-s 180NF (GE phoenix|x-ray, Germany). For the determination of length distributions especially for highly filled materials a high resolution is necessary. Therefore, a voxel edge length of 2 µm was chosen. This leads to a representation of fiber diameter by approximately 5 to 6 voxels.

Fiber length and orientation was determined by single fiber analysis. Start and endpoint of each fiber was determined by medial axis extraction followed by an analysis of connected points. Details of the method with an analysis of the achievable accuracy is published in a previous paper [30]. For the highly filled material containing 50 wt% fibers, the accuracy is lower than for the other materials since many fibers are very closely packed and the

separation procedure in some cases do not work perfectly. However, manual length measurements of ensembles of fibers from a 50 wt% sample gave only slightly higher average length (less than 10 % increase) so the accuracy is considered sufficient. The accuracy of the determined fiber orientation is not affected by this circumstance as much as fiber length. The average fiber diameter is approximately 11 μm. Fibers with length below 30 μm was considered as fragments and not included in the extracted data.

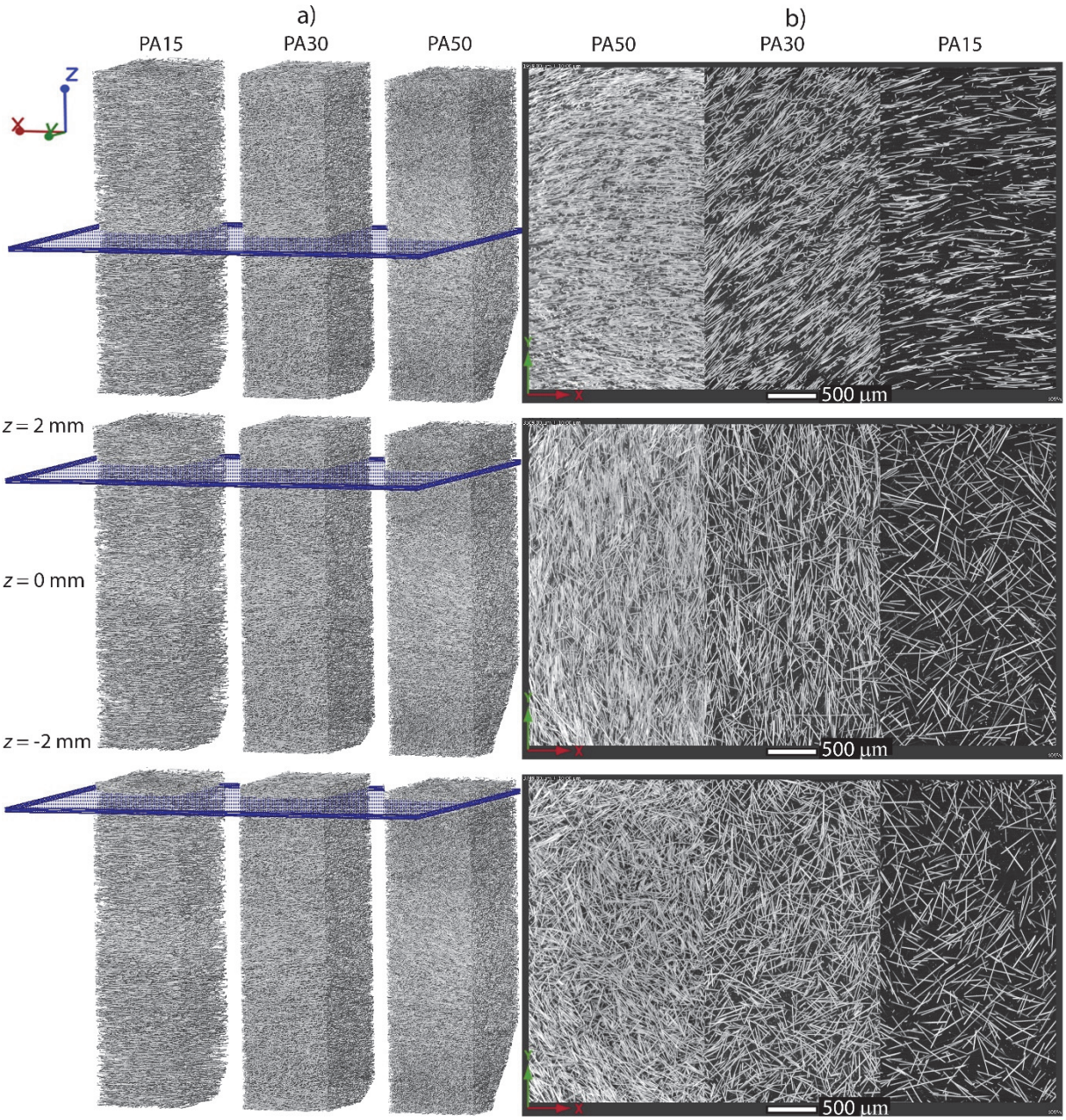

Figure 4 a) Reconstructed 3D volume data from CT scans at the 28 mm position for PA15, PA30 and PA50. b) View in the z direction of 20 µm thick volume slices of the data in a) at the position shown with blue planes in the adjacent pictures in a).

Results and discussion

Material properties

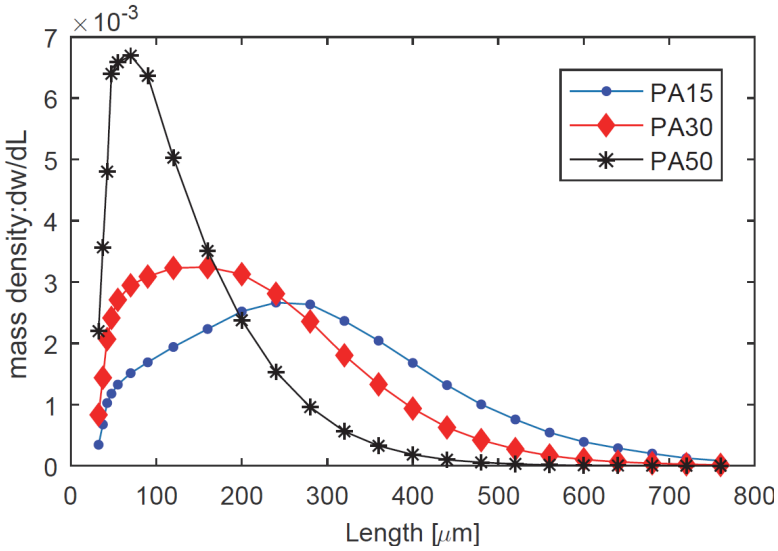

Figure 5 Length distributions of the fibers in PA15, PA30 and PA50.

Figure 4 shows examples of reconstructed volume data for the three fiber concentrations. It is notable that even for 15 wt% fiber concentration there is a considerable overlap between the fibers. For 50 wt%, and also to some extent for 30 wt% many fibers align in bundles.

Figure 5 shows the distributions of fiber lengths in the samples determined from analyses of the μ-CT data. The average fiber length clearly decreases with increasing fiber concentration. However, there is no trends in evolution of fiber lengths between different positions within the plates. Hence, either the materials have different initial fiber lengths, or fiber breakage occurs in the process before the material reaches the film gate. Since the fiber length values are constant within the plates, the reason for the difference in fiber length is not of direct importance for this study. Table 1 lists selected average characteristics of the fiber length and orientation data extracted form the μ-CT data. $<>_n$ and $<>_V$ designate number- and volume-weighted averages respectively. The volume-weighted average equals the mass-weighted average if fiber density is assumed constant. The detailed information about fiber orientation allows calculation of characteristics relevant for fiber interaction such as average spacing $<h_f>_V$, and from that the average particle number N_p^V (Equation 9), also listed in Table 1, can be obtained. The average spacing $<h_f>_V$ is calculated as follows:

- For every fiber i: Find the shortest distances from every point along the fiber to the nearest point on neighboring fibers. Find the average of these distance $h_{f,i}$

- Calculate $\langle h_f \rangle_V$ as the volume-average of $h_{f,i}$

N_p^V is calculated as the volume-weighted average of individual $N_{p,i}$ calculated from $h_{f,i}$ and L_i (length). It should be noticed that for all three materials the fiber volume fraction (*c)* is larger than the inverse fiber aspect ratio (a_r^{-1}) which means that all samples are concentrated fiber suspensions. In fact, more or less all fibers, except the shortest, are at some point along their axis in contact with or very close to another fiber. N_p^V is proportional to the square of fiber length. Hence, since the fiber length decreases with weight fraction, the N_p^V values for PA15 and PA50 are nearly the same, and N_p^V for PA30 is only slightly higher than for PA15 and PA50. N_p^V values only vary slightly between different sample positions and various positions through the thickness within each sample. Therefore, we only report one average value for each material. The fiber orientation results presented below clearly indicate an increasing fiber–flow coupling with increasing fiber content. This suggests that Equation 9, utilized to calculate N_p, which was deduced for idealized semi-concentrated fiber suspensions, can have limited validity for concentrated suspensions as examined here.

Table 1 Material characteristics obtained from μ-CT data. Subscript and superscript n and V denote number and volume average, respectively.

Material	wt% %	V% %	c m^3/m^3	$\langle L_f \rangle_n$ [μm]	$\langle L_f \rangle_V$ [μm]	$\langle ø \rangle$ [μm]	$\langle h_f \rangle_V$ [μm]	N_p^V	$\langle a_r^{-2} \rangle_V$	$\langle a_r^{-1} \rangle_V$
PA15	15.8	6.6	0.066	212	306	10.8	20.3	17.1	0.0012	0.0353
PA30	27.7	12.7	0.127	153	226	10.8	15.0	27.2	0.0023	0.0478
PA50	50.4	27.7	0.277	88	128	10.8	12.9	17.9	0.0071	0.0844

Flow characteristics

The experimental data were sampled along the symmetry line in the y direction, dividing the plate in two halves, see Figure 3. The orientations at these points are a function of the flow history starting at the nozzle. Down the sprue, fibers will be strongly oriented in the z direction. After the entrance to the plate cavity, the fibers will experience a radially diverging flow that is expected to orient the fibers in the xy plane with a core-shell structure. In the film gate the part thickness is reduced by 50 %, all along the edge of the 80 mm × 80 mm plate. The purpose of this gate is to retard the flow into the plate until the whole width upstream of the gate is filled. This should promote a flat flow front during filling of the plate to provide homogenous properties in the plate. In practice, the flow passes through the film gate at the

center before the edges resulting in a radially divergent flow front that becomes gradually flatter. Into the gate the flow contracts, followed by a short period of flow though the thin gate, ending with expansion into the plate cavity. This is expected to initially orient fibers in the xy plane and towards y direction. The expansion will orient fibers in the z direction, in particular in the bottom half of the cavity when viewed as in Figure 3. After this, there will be flow between two parallel plates, and a core–shell structure is expected to establish downstream. Since all samples, from y = 0 mm to y = 50 mm, are far from the end of the plate cavity, flow front effects are negligible for the final orientation, except for the fiber orientation at the skin, where material is deposited directly by fountain flow.

Measured fiber orientations

A visual overview of the fiber orientation for all the samples can be obtained by projections of the "FO crosses" onto yz planes, as shown in Figure 6. The drawing on the top shows the sample positions in the plate corresponding to each square block of "tensor crosses" in the three diagrams below. The "tensor crosses" mostly appear as lines or points. If the projection of the "tensor cross" appears as a line the degree of orientation is large in the line direction. The "tensor crosses" appear as points when the orientation in x direction is dominant. The color code for the "tensor crosses" are, red, blue and green for first, second and third principal direction, respectively.

First to notice in Figure 6 is the differences in orientation already just after the gate. As expected, the contraction due to the gate orients the fibers in the y direction. In the “0 mm” sample of PA15, there is a band of high y orientation, going from the lower half of the gate to the plate core at the end of the sample. PA30 and PA50 have similar oriented bands from the gate to the plate core. However, apart from these initial bands, the orientations for PA30 and PA50 in the “0 mm samples” differs markedly from PA15. At the top surface (straight forward from the gate), a high y orientation exists for PA30 and PA50 while it is much lower for PA15. In addition, in the corner below the gate, when viewed as in Figure 6, a triangular area with high x orientation is formed for PA30 and PA50. The high y orientation straight forward from the gate and the observed orientations in the corners are qualitatively in accordance with previously reported observations for die exits; high fiber content polymers generate straighter flow lines and larger corner vortexes [21, 26, 27].

Further downstream, a core-shell structure builds up. For PA15 the transverse to flow (x) oriented core layer is thin and the remaining sample has a rather random distribution in the xy

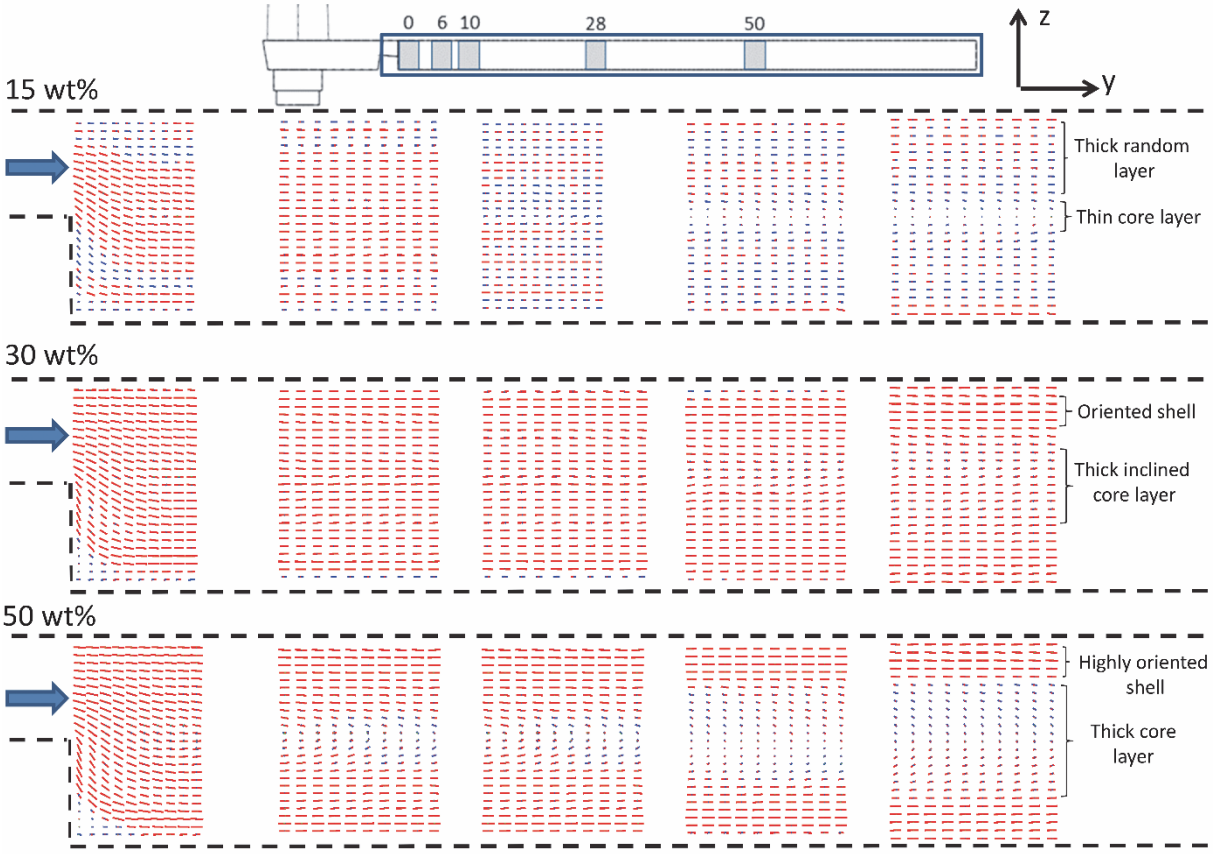

Figure 6 yz slice views of fiber orientations using principal orientation "tensor crosses". The drawing on the top shows the five sample positions in the plate corresponding to each square of "tensor crosses" in the three diagrams below. The three diagrams (one for each material) show the projection of "tensor crosses" onto the yz plane. The color code for the "tensor crosses" are, red, blue and green for first, second and third principal direction, respectively.

plane. Contrary to this, the core layer for PA50 is thick, and outside the thick core the fibers are mainly oriented along the flow direction (y). Apparently, from the yz projections in Figure 6, a distinct core-shell structure does not develop for PA30. However, examining the "tensor crosses" of PA30 in perspective view as shown in Figure 7, reveals that a highly oriented core layer develops, but this core layer is aligned along an axis inclined between the x and y axes. Outside the core, fibers are primarily oriented in the flow direction (y). The same type of perspective view is shown for the 50 mm for all three fiber content in Figure 8.

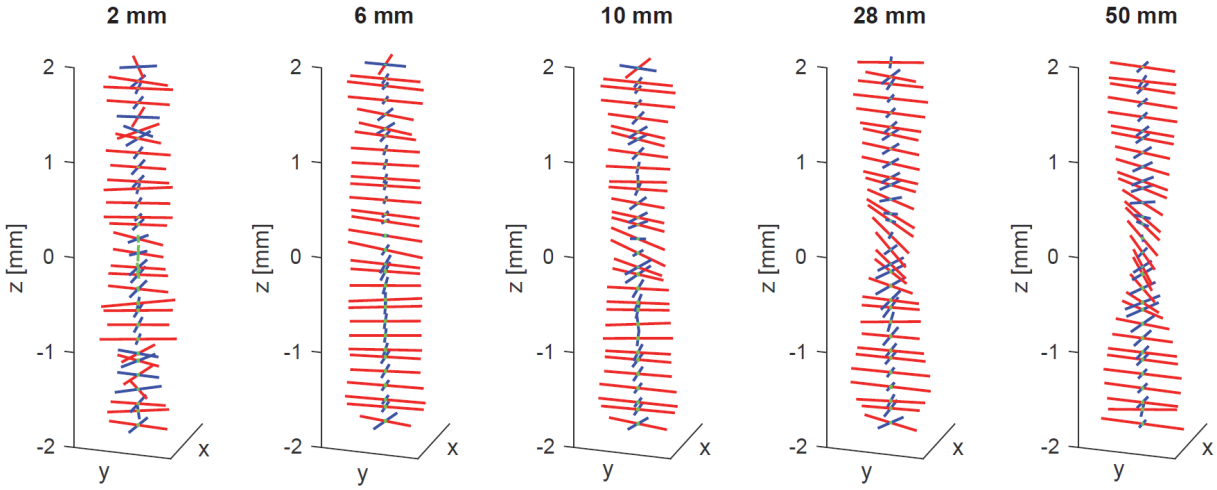

Figure 7 Perspective view of PA30 "orientation tensor crosses" at 2, 6, 10, 28 and 50 mm downstream from the gate. The third principal orientation component (green line) is generally small and only seen near the center in some of the plots.

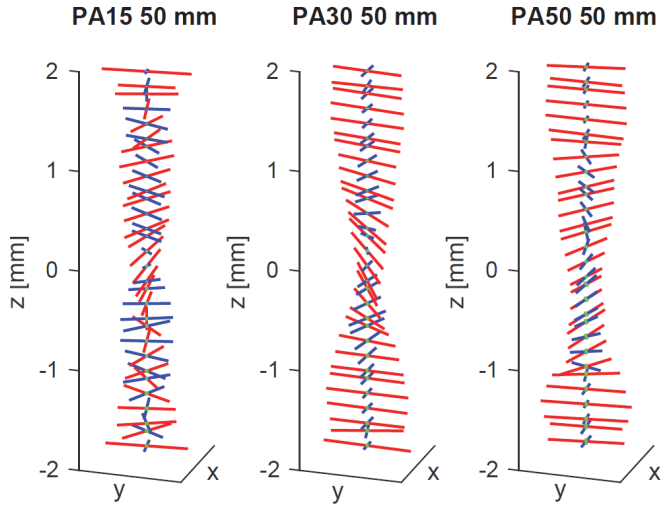

Figure 8 Perspective view of "orientation tensor crosses" 50 mm downstream from the gate for PA15, PA30 and PA50.

Additional insight into the differences between the samples can be obtained from plots of values of individual tensor components through the thickness. Figure 9 and Figure 10 show the orientation tensor components in the sample coordinate system.

Figure 9 shows the diagonal components of the orientation tensor and Figure 10 shows the off-diagonal components. Since the orientation varies considerably just after the gate, orientation tensor data from the inlet sample are calculated from the range [2 mm < y < 2.5 mm] and referred to as "2 mm". For the other positions, data are calculated for the whole sample. As discussed above, the fiber orientations just after the gate are quite complex.

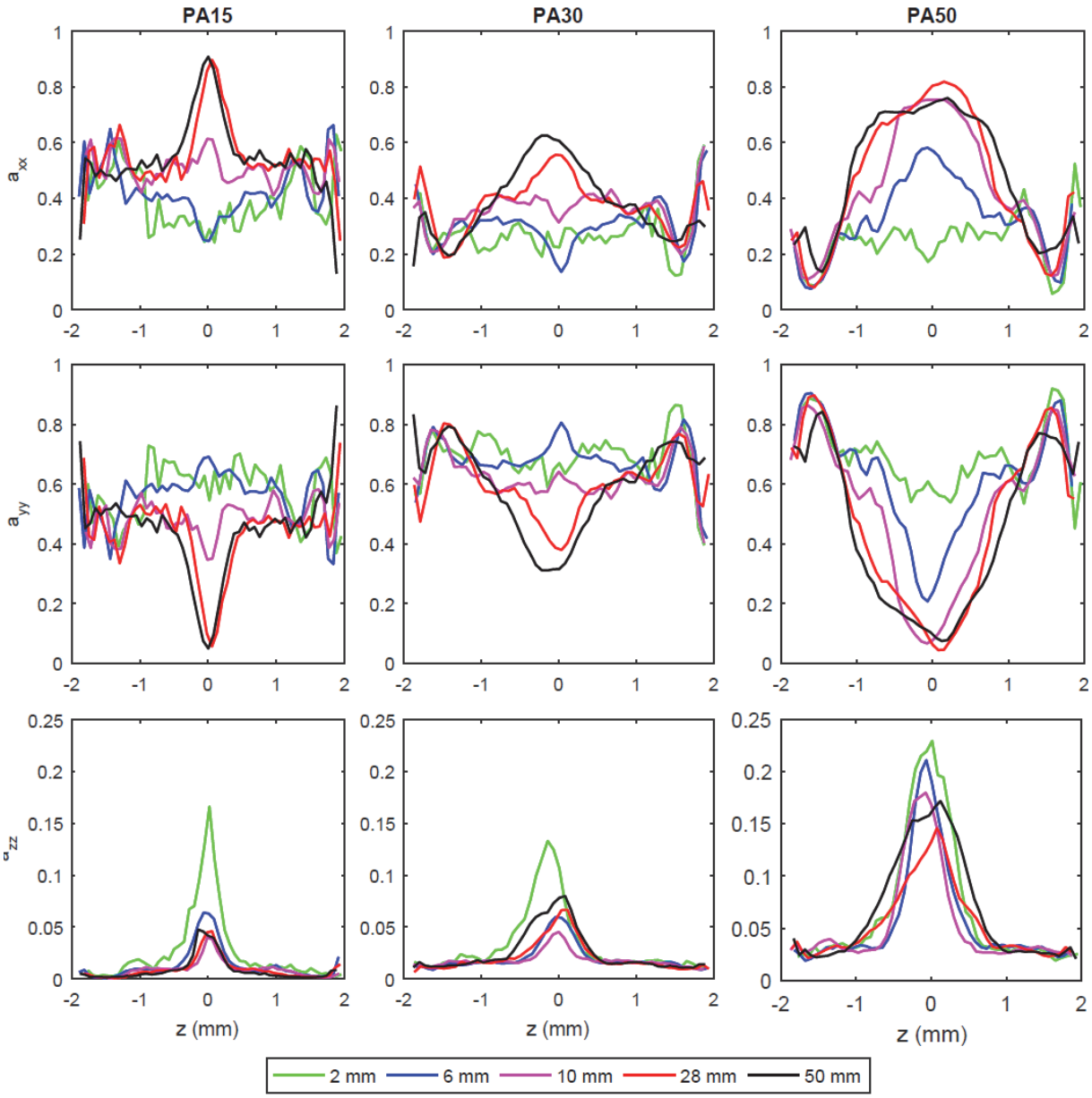

Figure 9 Diagonal fiber orientation tensor components with respect to the sample coordinate axes for PA15, PA30 and PA50

However, already after approximately 2 mm from the gate, the fiber orientations become close to symmetric around the mid plane of the plate for all three materials. Notably, with some exceptions near the skin, the fiber orientations at 2 mm are rather similar for the three fiber contents. This is a useful observation with regard to the intention of comparing downstream evolution of fiber orientation in the three cases.

Considering the PA15 material, the orientation just after the gate (2 mm) is close to random in the xy plane all through the thickness, with a slight preference of orientation in the flow

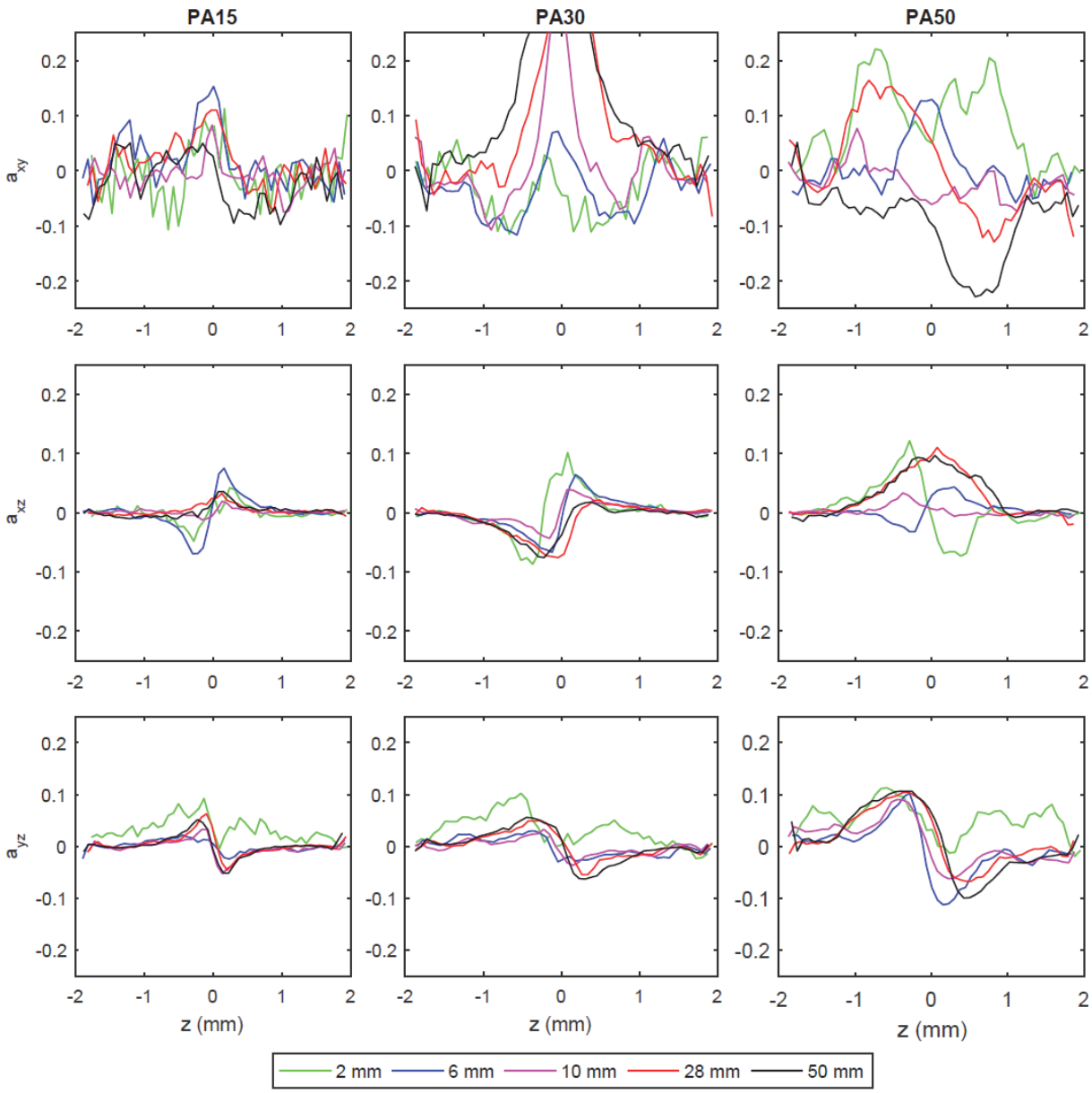

Figure 10 Off-diagonal fiber orientation tensor components with respect to the sample coordinate axes for PA15, PA30 and PA50.

direction (y). Going from 2 to 6 mm the orientation tends to become slightly more evenly distributed between x and y directions, except at the mid-plane where a higher y orientation is preserved. At 10 mm the fiber orientation is close to random in the xy plane, except from the appearance of a thin y oriented skin layer and a thin x oriented core layer. The z component has a rather high value at 2 mm, but quickly reduces and reaches a steady state at 10 mm. Going from 10 mm to 28 mm the major change is the formation of a distinct transverse-to-flow (x) oriented core layer. The fiber orientation values at 28 and 50 mm are identical and can be considered as steady state values. The steady state orientation for PA15 is

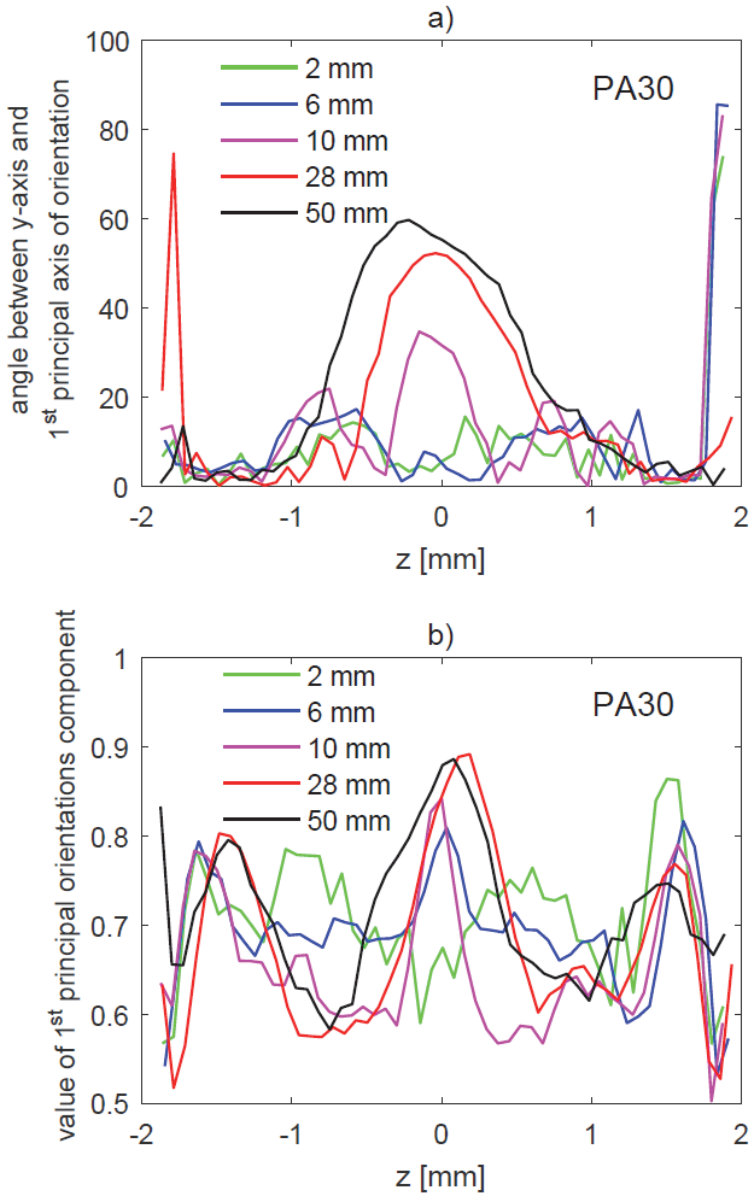

Figure 11 For PA30: a) The angle between the y axis and the first principal direction. b) The value of the 1st principal orientations component.

characterized by a distinct 0.5-0.7 mm thick transverse-to-flow (x) oriented core layer, a thick transition layer with a random fiber orientation distribution in the xy plane and no distinct shell layer before the skin layer. This absence of a shell layer is notable. Out-of-plane (z) orientation is small and most evident in the core layer. With regard to simulations with the FT model and its extensions discussed above, this calls for a very high anisotropic rotary diffusion coefficient from the shear flow direction (y) towards the transverse (x) direction.

PA30 and PA50 differ significantly from PA15, indicating significant concentration effects. PA30 at 2 mm is, as PA15, characterized by a rather uniform orientation through the thickness

and a principal direction of orientation parallel to flow (y) throughout the thickness. Also, as for PA15, but more distinct, a y oriented core layer appears at 6 mm. The reason for this y aligned core layer is difficult to state. One explanation could be that some extensional flow occurs in the y direction when the flow lines change from diverging to parallel between 0 and 6 mm. Contrary to PA15, PA30 shows a distinct shell layer already at 6 mm. Due to the angle between the dominant direction of the fiber orientation in the core layer and the x and y axes (cf. Figure 7), it is difficult to interpret the tensor components with reference to the xyz coordinate system. To compensate for this, data are shown in an alternative form in Figure 11. Figure 11 shows the angle between the y axis and the first principal direction, and the value of the 1st principal orientations component. In the shell layer the angle is close to zero changing to 50-60 degrees for the core region. The plots in Figure 11 reveal the typically observed layer structure including a highly oriented core, a randomly oriented transition layer, a flow-aligned shell layer and a randomly oriented skin layer. The maximum degree of alignment in the core is close to the one found for PA15, but the core layer is

approximately 50 % thicker. The z orientation is slightly higher than for PA15, but beside that it shows a similar pattern with larger a_{zz} values in the core layer and near the gate. Downstream from the gate, the z orientation is quickly reduced to a steady state profile.

Increasing the fiber content further to 50 wt% brings on additional changes in the fiber orientation. For PA50, distinct shell layers with very high fiber alignment in the y direction are formed just after the gate, and these layers are retained downstream in the plate. As also seen in Figure 6, a notable characteristic of PA50 is the very broad core layer with a rather high out of plane (z) orientation component. The transversely (x) oriented core layer makes up half the thickness of the sample (2 mm), and it is already significantly evolved 6 mm from the gate. Consequently, the transition layer is very thin. As for PA15 and PA30 the z component is high near the gate, but contrary to those two cases, for PA50 the peak a_{zz} value is only moderately reduced and a_{zz} actually grows at the borders of the core region as the core widens downstream. The orientation is close to a steady state from 28 mm and further downstream. The major difference between 28 mm and 50 mm is that the a_{zz} peak is broader and higher at 50 mm for PA50, as seen in Figure 9. In summary, with a higher fiber concentration the core becomes thicker and the shell layers become more oriented in the flow direction.

The reason for the inclined core layer for PA30 is difficult to state. The shell layers have fibers aligned along the y axis, so the overall flow direction must be in the y direction. The

core layer orientation is not random in the xy plane (as for some film gated strips [5]) so the core layer orientation must be related to extensional flow transverse to the filling direction. Consider a number of fibers, highly aligned along a reference axis, being subjected to a transverse extensional flow. The extensional flow will rotate the fibers towards the transverse direction. This rotation can occur in two directions, say right or left. In the ideal case, half of the fibers turns right and the other half turns left. During rotation, the orientation tensor component in the transverse direction will increase, but since an equal number of fibers is inclined in both directions, the off-axis tensor component will cancel to zero. In reality, the flow in injection molding will be subject to disturbances and inhere some degree of random characteristics. Hence, even for a simple geometry like a film gated plate the extensional flow is not perfectly perpendicular to the main flow direction (y). With some angle between the extensional flow and the transverse (x) direction, a major part of the fibers will rotate in one direction towards alignment with the extensional flow. Fiber–fiber interaction will likely also enhance mutual reorientation. The inclination of the core only changes slightly from position 28 mm to position 50 mm. This must be due to plug flow and nearly parallel flow lines (flat flow front) from 28 mm and beyond, resulting in very small strain rates in the core.

The core layer for PA50 also has the tendency of inclination though not as consistently as for PA30. The xy component of the PA50 orientation tensor in the upper right corner of Figure 10 shows the following: At 6 mm the core layer is slightly inclined; at 10 mm close to perfectly transverse; at 28 mm one half is inclined approximately 15 degrees and at 50 mm the other half is inclined approximately 15 degrees to the opposite direction. For PA50 at 50 mm this is also visualized in Figure 8.

In total, it appears as the local flow field becomes more irregular and unstable with increasing fiber content. In practice, this is seen when examining short shots of highly filled materials, typically having irregular flow front with clear signs of viscous fingering.

The authors have observed inclined core layers in analyses of other parts, but has no statistics on this phenomenon. If it has a random nature, averaging of orientation from replicate samples from the same cavity should level out the inclination.

The higher fiber alignment in the shell layer for higher fiber concentrations, supports earlier findings [5] suggesting that low interaction coefficients C_I should be used for simulating materials with high fiber concentration.

The measured fiber orientation challenges the common rule of thumb that orientation in the filling direction dominates the overall fiber orientation. Figure 12 shows the through-the-thickness averages of the orientation tensor components a_{xx} and $a_{yy,}$ as a function of distance from the gate. For PA15 and PA50 the orientation transverse to filling is just as high, and in some cases higher, than in the filling direction. This is caused by the thick random layers in PA15 and the thick transversely oriented cores in PA50.

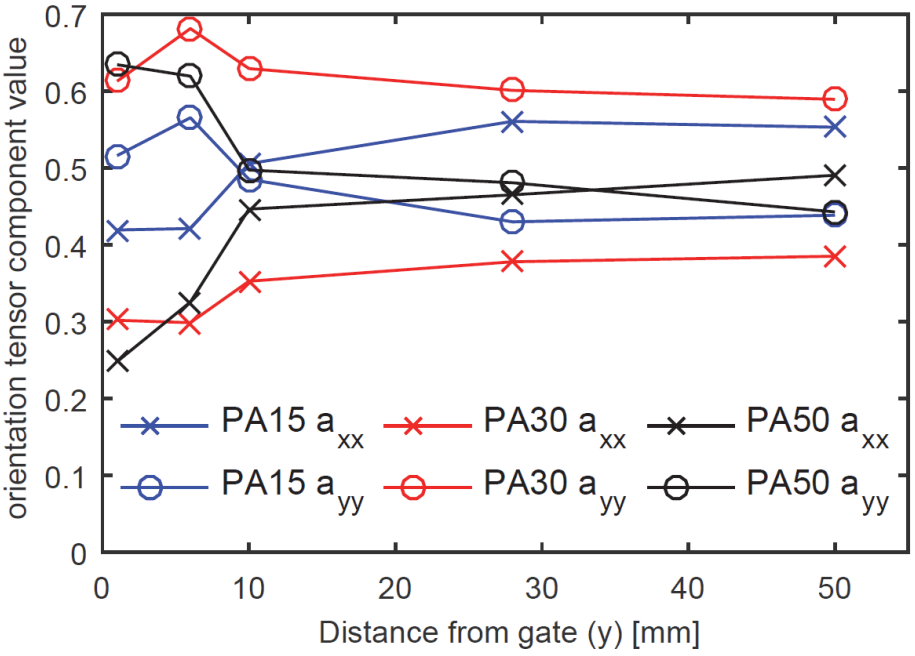

Figure 12 Through-the-thickness averages of a_{xx} and a_{yy} orientation tensor components as a function of distance from the gate.

Fiber length dependence

Since the μ-CT analyses includes a simultaneous determination of both fiber length and orientation, the data allow binning and plotting of the orientation parameters for different ranges of fiber lengths. Figure 13 shows a_{xx}, a_{yy} and a_{zz} for different ranges of fibers lengths. (Due to the fiber length distribution, data are quite scattered for the shortest fibers in PA15 and the longest fibers in PA50). For clarity, only data for the 50 mm position are displayed. The data show that the z component in the shell and transition layers increases significantly with decreasing fiber length. This tendency is qualitatively the same for all fiber concentrations. This is in good agreement with Jeffery's model (Equation 5) that predict that the orientation perpendicular to the shear plane (i.e. in the z direction) increases with decreasing fiber aspect ratio. Another interesting observation is that, in the shell and transition

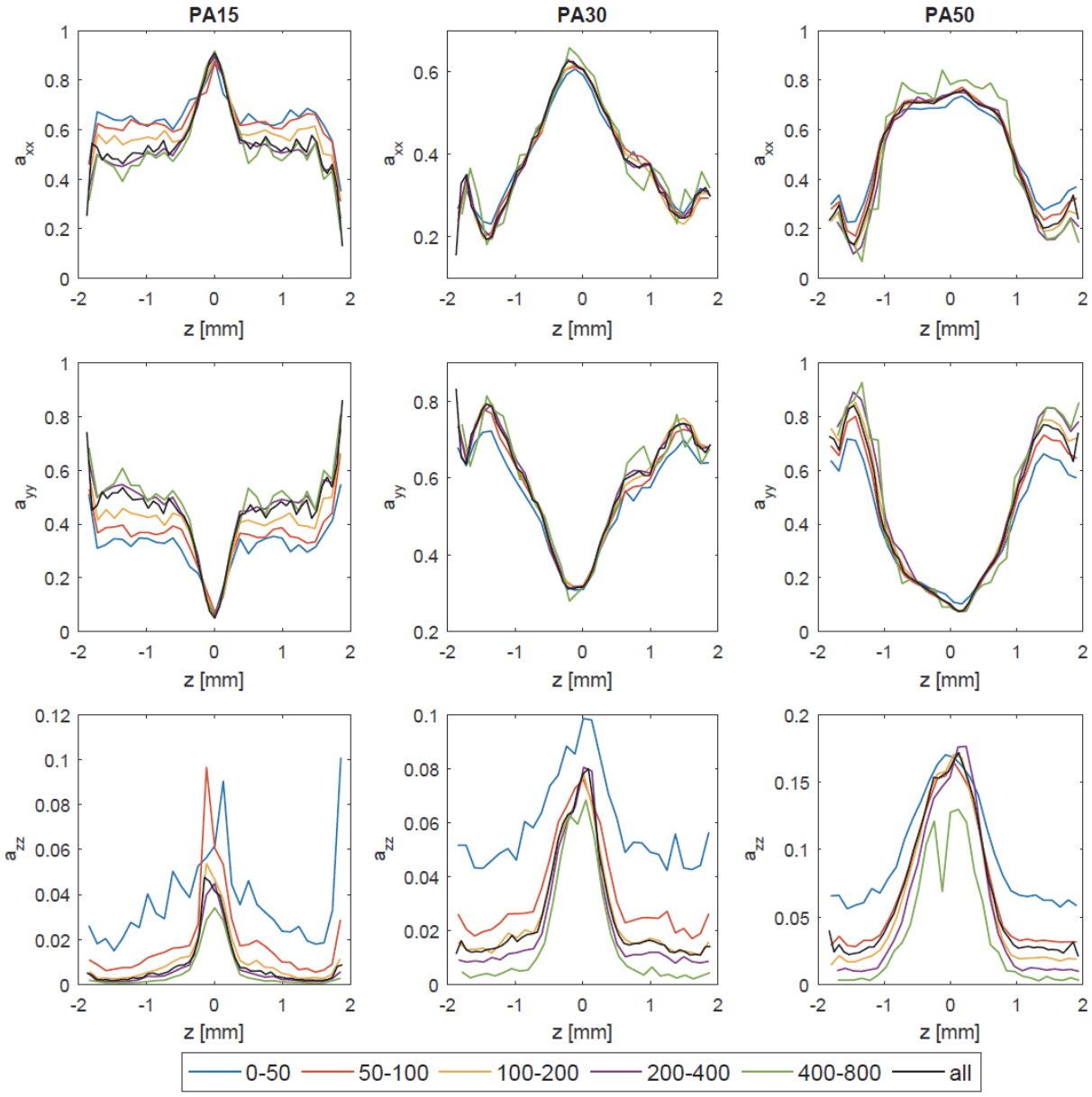

Figure 13 a_{xx}, a_{yy} and a_{zz} for different fiber length intervals (in the range 0-800 micrometers) within the same sample for PA15, PA30 and PA50 samples located 50 mm away from the gate.

layers, the degree of transverse (x) orientation increases with decreasing fiber length. This is most evident for PA15 and PA50. For the shortest fibers in PA15, transverse orientation is actually dominant. Comparison with other sample positions shows that this is close to a steady state. This dominant transverse orientation is contrary to what is predicted by all the models discussed previously in this paper. However, these models only consider an average aspect ratio and not a fiber length distribution. The fiber orientation driving force is a result of the macroscopic flow field and stochastic fiber–fiber interactions on micro scale that reduces

the local degree of alignment. It is plausible from a mechanistic point of view and supported by the data in Figure 13, that in a suspension of fibers with varying length the shortest fibers are more prone to be oriented due to stochastic processes than the longest fibers. To the authors' knowledge, this type of length resolved orientation data have not previously been published. Hence, additional studies need to be performed to verify these observations and hypotheses in general.

Observation of the flow is not included in this study, but the observed fiber orientation trends provide strong indication that the flow field is significantly influenced by the fibers for high fiber concentrations. The fiber orientation found for PA15, with a relatively thin core layer and a thick layer with random orientation from core to skin, indicates a flow with a gradually changing shear gradient from the wall to the "shear free" center line. The z orientation component is very small everywhere except in the core. As a result, the extra stress from fibers in the sheared zones is expected to be small. Thus, for PA15, fiber–flow coupling appears to be negligible and it seems reasonable to omit it in modelling. In order to obtain the thick random layer a model with high anisotropic rotary diffusion, providing diffusion only in the shear plane, would be sufficient.

The fiber orientation in PA30 and PA50 is in accordance with a plug flow with strong shear gradients in a well-defined region near the cavity wall and a vortex at the inlet corner. These trends become more evident with increasing fiber concentration and are likely a result of a significant fiber–flow coupling.

The flow in the plate upstream from the flow front is dominated by shear flow that can be approximated as a simple yz shear flow with varying rate through the thickness (z). In the core, deformation rates are low and transverse extensional flow can dominate. Assuming only simple yz shear, the shear rate and velocity profile through thickness will depend on the effective shear viscosity η_{yz}, which from Equation 7 and Equation 8 is theoretically given as

$$\eta_{yz}^{eff} = \eta\left(1+2N_p A_{yzyz}\right) \tag{10}$$

Examination of $\eta_{yz}/\eta = 1+2N_pA_{yzyz}$ through the thickness should indicate the influence of fibers on the viscosity that governs the flow field. Our calculations of N_p, as described in the materials properties section, showed only insignificant variation of N_p through the thickness of the plates. In addition, the variation between PA15, PA30 and PA50 was rather small (17-

27) with no clear trend. Hence, N_p is assumed to be constant in the following discussion and

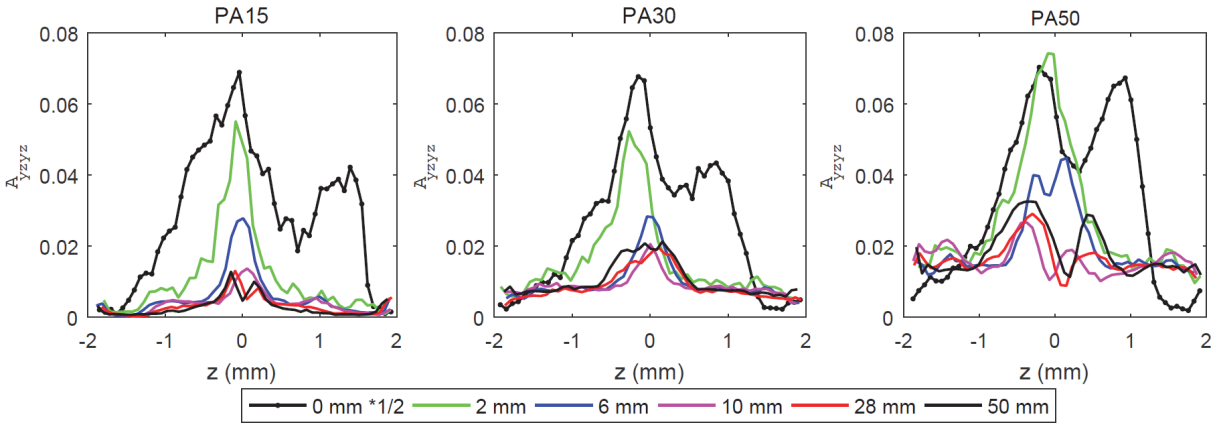

Figure 14 The A_{yzyz} component of the fourth order orientation tensor. The effective viscosity enhancement for simple shear in the filling direction is given as $\eta_{yz}/\eta = 1+2N_pA_{yzy}$. To reduce the axis scale 0.5× A_{yzyz} is plotted for "0 mm".

A_{yzyz} is plotted as a measure of fiber–flow interaction in Figure 14. The reader can readily calculate the viscosity enhancement factors η_{yz}/η from the plotted data and any desired N_p value. In Figure 14 A_{yzyz} is plotted for two sub-volumes of the inlet samples. "0 mm" is calculated from the range [0 mm < y < 0.5 mm] and "2 mm" is calculated from the range [2 mm < y < 2.5 mm] as in the previous figures. To reduce the axis scale 0.5× A_{yzyz} is plotted for "0 mm". At "0 mm" the flow cannot be approached as simple shear. The "0 mm" data are included to compare the starting conditions. A_{yzyz} at "0 mm" is actually very similar in the three cases. For PA15 A_{yzyz} rapidly decreases to low values except in a thin core layer. In the outermost 1 mm A_{yzyz} nearly vanishes completely. For PA30 and PA50 steady state values are, as for PA15, rapidly established outside the core region, with highest values for PA50. The widths of the center peaks are rather constant for all the samples, but the values fluctuate. The peak widths and magnitudes increase with fiber content. The increase of A_{yzyz} (as well as a_{zz}, see Figure 9) with concentration in the shell and transition layers can be attributed to the decrease in fiber length with concentration through Equation 5. The high values of A_{yzyz} in the wide center part for PA30 and in particular for PA50, will according to the Dinh – Armstrong model (Equation 8) promote plug flow that again promote a wide core region as a positive feedback for continued plug flow. That argument supports the Dinh – Armstrong model. On the other hand, since A_{yzyz} at 0 mm is similar for all three concentrations and N_p is estimated to be similar for the three fiber contents, the Dinh – Armstrong model would predict a similar flow pattern and fiber orientation in the three cases, contrary to what is observed. Hence, it can also be argued, that differences in core width are a result of plug flow promoted by high

fiber concentration by mechanisms that are not described by the Dinh – Armstrong model. The Dinh – Armstrong model and the formula for N_p was developed for dilute and semi-concentrated fiber suspensions assuming no fiber-fiber contacts. Fiber-fiber contact is significant for the materials studied here. Alternative models, or alternative formulas to determine N_p accounting for the density of fiber–fiber contacts appears to be required to better capture the difference in rheology for concentrated fiber suspensions.

Summary and conclusions

The fiber orientation in injection molded film gated plates molded with PA12 with 15, 30 and 50 wt% fibers has been studied by μ-CT of a series of samples. The fiber orientation is strongly dependent on fiber concentration. Increased fiber content results in

- Considerably thicker core layer and narrower transition layers
- Increased fiber alignment in the shell layer.
- Increased evidence of corner vortex after the gate.
- More irregular fiber orientation.

The observed fiber orientation indicate that increased concentration of fibers changes the flow pattern towards

- Plug flow with a thin highly sheared shell layer and a thick core region dominated by transverse flow, but in general low flow rates in the core.
- Larger corner vortex after the film gate.
- More irregular flow i.e. with more viscous fingering.

The observed fiber orientation and qualitatively deduced flow patterns are in good agreement with simulations including strong fiber flow interaction reported by several authors.

The results show that fiber concentration indeed can influence flow and fiber orientation dramatically and that fiber-flow coupling cannot be neglected in general. The steady state shear viscosity curves, $\eta(\dot{\gamma})$, commonly used in simulations are only weakly dependent on fiber concentration. Anisotropic rotary diffusion and add-ons to the Folgar – Tucker model retarding the flow are useful contributions to enable better modelling of fiber orientation dynamics, but do not alter the flow. It is therefore very unlikely that the differences in fiber orientation observed in this study can be modelled without including fiber-flow coupling. All injection molding simulation studies known by the authors including fiber-flow coupling have

utilized the Dinh – Armstrong model with the N_p factor dependent on fiber length and fiber-fiber spacing as a measure of degree of coupling. N_p values for the three concentrations estimated from averages of individual fiber lengths and fiber-fiber spacing only differ slightly, and will not provide the difference in flow that the observed orientations indicate. Efficient employment of fiber-flow coupling in engineering will require improved understanding of how to determine appropriate N_p values from experimental procedures or analyses of fiber morphology, i.e. with μ-CT.

μ-CT with detailed data analyses as presented here is a powerful tool for determining fiber orientation and length. It was shown based on the μ-CT data, that fiber dynamics is dependent on fiber length as predicted by Jeffery's model. Future studies of the effect of fiber concentration on flow and fiber orientation should aim at having equal fiber length to ease interpretation of results.

Acknowledgement

This study has been financed by the Eskomp project supported by the Research Council of Norway, Grant nr. 219526.

References

1. P. Laure, L. Silva and M. Vincent, in *Composite Reinforcements for Optimum Performance*, edited by P. Boisse, pp. 616-650, Woodhead Publishing, Oxford (2011)
2. S. G. Advani and C. L. Tucker III, *J. Rheo.*, **31**, 751 (1987).
3. S. M. Mazahir, G. M. Vélez-García, P. Wapperom and D. Baird, *J. Non-Newt. Fluid Mech.,* **216**, 31-44 (2015).
4. M. Vincent, T. Giroud, A. Clarke and C. Eberhardt, *Polymer,* **46** (17), 6719-6725, (2005).
5. R. S. Bay and C. L. Tucker, *Polym. Compos*., **13** , 332, (1992).
6. G. B. Jeffery, *Proc. R. Soc. London A*., **102**, 161, (1922).
7. M. Junk and R. Illner, J. Math. *Fluid Mech.*, **9** , 455, (2007).
8. F. Folgar and C. L. Tucker, *J. Reinf. Plast. Comp.* **3** , 98, (1984).
9. N. Phan-Thien, X. J. Fan, R. I. Tanner and R. Zheng, *J. Non-Newt. Fluid Mech.* **103**, 251, (2002).
10. J. H. Phelps and C. L. Tucker Iii, *J. Non-Newt. Fluid Mech.* **156**, 165, (2009).
11. H. M. Huynh, *Improved fiber orientation predictions for injection-molded composites*, Thesis University of Illinois at Urbana-Champaign, 2001.
12. M. Sepehr, G. Ausias and P. J. Carreau, *J. Non-Newt. Fluid Mech.* **123**, 19, (2004).
13. J. Wang, J. F. O'Gara and C. L. Tucker Ii, *J. Rheo.* **52**, 1179, (2008).
14. S. Kleindel, D. Salaberger, R. Eder, H. Schretter and C. Hochenauer, *Int. Pol. Process.* **30**, 366, (2015).
15. S. M. Mazahir, G. M. Vélez-García, P. Wapperom and D. Baird, *Composites A: Appl. Sci. Man.* **51**, 108, (2013).
16. K. J. Meyer, J. T. Hofmann and D. G. Baird, *Composites A: Appl. Sci. Man.* **62**, 77, (2014).

17. B. N. Nguyen, X. Jin, J. Wang, J. H. Phelps, C. L. Tucker III et al., *Implementation of New Process Models for Tailored Polymer Composite Structures into Processing Software Packages*. DOE-report PNNL-19185, 2010.
18. H. C. Tseng, R. Y. Chang and C. H. Hsu, *J. Rheo.*, **57**, 1597, (2013).
19. H.-C. Tseng, R.-Y. Chang and C.-H. Hsu, *J. Rheo.*, **60**, 215, (2016).
20. E. G. Kim, J. K. Park and S. H. Jo, *J. Mater. Process. Technol.* **111**, 225, (2001).
21. G. G. Lipscomb Ii, M. M. Denn, D. U. Hur and D. V. Boger, *J. Non-Newt. Fluid Mech.* **26**, 297, (1988).
22. S. M. Dinh and R. C. Armstrong, *J. Rheo.*, **28**, 207, (1984).
23. H. M. Laun, *Colloid Polym. Sci.* **262**, 257, (1984).
24. A. P. R. Eberle, G. M. Vélez-García, D. G. Baird and P. Wapperom, *J. Non-Newt. Fluid Mech.* **165**,110, (2010).
25. C. L. Tucker Iii, *J. Non-Newt. Fluid Mech.* **39**, 239, (1991).
26. B. E. VerWeyst and C. L. Tucker, *Can. J. Chem. Eng*., **80**, 1093, (2002).
27. A. Redjeb, P. Laure, L. Silva, M. Vincent and T. Coupez, in *PPS-21 (Leipzig, Germany, June 19-23 2005)* (Leipzig, 2005).
28. S. T. Chung and T. H. Kwon, *Polym. Compos.* **17**, 859, (1996).
29. D. H. Chung and T. H. Kwon, *J. Non-Newt. Fluid Mech.* **107**, 67, (2002).
30. D. Salaberger, M. Jerabek, T. Koch and J. Kastner, in *Mater. Sci. Forum*, Vol. **825**, 907, (2015).